
# Reducing plastic anisotropy through stress induced martensitic transformation in an additively manufactured metastable medium entropy

Materials Science & Engineering A 933 (2025) 148308

Contents lists available at ScienceDirect

Materials Science & Engineering A

journal homepage: www.elsevier.com/locate/msea

# Reducing plastic anisotropy through stress induced martensitic transformation in an additively manufactured metastable medium entropy alloy

Sri Bala Aditya Malladi [a,*], Tatiana Mishurova [b], Vishnu Anilkumar [a], Bharat Mehta [a,f], Alexander Evans [b], Kumar Babu Surreddi [c], Malte Blankenburg [d], Ulrich Lienert [d], Giovanni Bruno [b,e], Sheng Guo [a], Lars Nyborg [a]

[a] Department of Industrial and Materials Science, Chalmers University of Technology, SE-41296, Göteborg, Sweden
[b] Bundesanstalt für Materialforschung und–prüfung (BAM), Unter den Eichen 87, 12205, Berlin, Germany
[c] Department of Engineering Sciences and Mathematics, Materials Science, Luleå University of Technology, 971 87, Luleå, Sweden
[d] Deutsches Elektronen-Synchrotron (DESY), Notkestr. 85, D-22607, Hamburg, Germany
[e] Institute of Physics and Astronomy, University of Potsdam, Karl-Liebknecht-Straße 24-25, Potsdam, 14476, Germany
[f] Department of Materials Science and Engineering, KTH Royal Institute of Technology, Brinellvägen 23, Stockholm, 10044, Sweden

ARTICLE INFO

*Keywords:*
Powder bed fusion-laser beam
Medium entropy alloys
Phase transformation
Load partitioning
Synchrotron X-ray diffraction

ABSTRACT

Powder bed fusion laser beam (PBF-LB) is particularly effective for fabricating compositionally complex alloys such as high-entropy alloys (HEAs) or medium-entropy alloys (MEAs). Fabricating non-equiatomic metastable MEAs using PBF-LB can lead to the formation of unique microstructures that enhance the mechanical performance of these alloys. Nevertheless, plastic anisotropy in materials prepared by additive manufacturing routes including PBF-LB remains to be a technical challenge. This work presents the fabrication of a metastable non-equiatomic $Co_{45}Cr_{25}(FeNi)_{30}$ MEA using PBF-LB. As-printed samples exhibited the formation of nano-scaled ε-martensite (HCP) phase along with the FCC phase. The HCP phase exhibited Shoji-Nishiyama orientation relationship with the FCC phase. High energy synchrotron X-ray diffraction (HEXRD) and electron backscatter diffraction (EBSD) in-situ tensile testing were employed to investigate the influence of the HCP phase on the alloy's deformation behavior. The presence of the HCP phase initiates stress-induced martensitic transformation well below the macroscopic yield strength. This transformation led to the non-linear stress and strain response for the FCC phase. Further straining resulted in significant load partitioning, with the HCP phase taking the majority of the load as it formed, significantly strain hardening the alloy and reducing the plastic anisotropy induced by texture in the as-printed material.

## 1. Introduction

High entropy alloys (HEAs) and medium entropy alloys (MEAs) have attracted increasing attention from the scientific community over the last two decades. The unique alloying concept is to have multiple principal elements in equiatomic or near equiatomic proportions. This strategy leads to the entropy stabilization of simple solid solution phases [1–5]. This resulted in the development of prototype HEAs and MEAs such as CoCrFeMnNi and CoCrNi, which exhibit excellent combinations of strength and ductility, as well as enhanced fracture toughness at room and even more so at cryogenic temperatures [6–17]. The mechanism for improved properties of such alloys at cryogenic temperatures is thought to be the change in the dominant deformation modes from dislocation slip at room temperature to deformation twinning at cryogenic temperatures, as the stacking fault energy (SFE) of the alloys decreases with decreasing temperature.

SFE is an intrinsic material property that significantly influences the deformation behavior of an alloy. Typically alloys with high SFE tend to undergo deformation through dislocation slip, alloys with medium SFE undergo twinning upon deformation, and those with low SFE energy are known to undergo phase transformation [18–20]. Transformation induced plasticity (TRIP) typically refers to the transformation of a

* Corresponding author.
*E-mail address:* malladi@chalmers.se (S.B.A. Malladi).

https://doi.org/10.1016/j.msea.2025.148308
Received 29 October 2024; Received in revised form 17 March 2025; Accepted 7 April 2025
Available online 8 April 2025

metastable phase into a more stable phase upon deformation. Load partitioning in alloys that undergo TRIP refers to how stress and strain are distributed among different phases that are present in the microstructure upon deformation. The microscopic distribution of stress and strain among different phases defines the macroscopic mechanical response of these alloys [21–23].

Lately, there is a growing interest in the field of HEAs to explore the potential of non-equiatomic HEAs by engineering SFE to produce alloys with improved strength (without compromising ductility), and improved damage tolerance [17–20,24–31]. The microstructure typically consists of a single metastable FCC phase, which upon deformation transforms to a more stable ε-martensite (HCP) phase.

Additive manufacturing (AM) refers to the plethora of manufacturing techniques which manufacture components in a bottom-up approach layer-by-layer, as opposed to the traditional top-down approach to manufacturing (subtractive). Among the available AM techniques, powder bed fusion – laser beam (PBF-LB) is one of the most widely used technologies. It uses high energy laser as a power source to selectively melt thin layers of powder which rapidly solidify to produce near net shape components. This produces unique hierarchical microstructures of the components due to high cooling rates and high thermal gradients inherent to the technique [32]. The rapid melting and solidification process taking place layer after layer also results in the subsequent thermal cycling, generating a high density of dislocations in the as-printed state [33,34]. The high cooling rates in the PBF-LB also result in minimal elemental segregation, which suppresses the formation of secondary phases that could be detrimental to the performance of the alloys. In some alloy systems, the high cooling rates also result in the formation of martensitic phases in the as-printed state, which could enhance the mechanical properties of the fabricated alloys [35]. These unique characteristics of PBF-LB are attractive for the fabrication of HEAs and MEAs with good homogeneity and reproducibility. The production of such alloys would be otherwise quite laborious or even impossible if one would use conventional manufacturing techniques like arc or induction melting, since subsequent thermomechanical treatments, i.e., cold or hot deformation followed by heat treatments, are necessitated but difficult to implement for complex geometries.

The target alloy in the present study is based on the $Co_xCr_{25}(FeNi)_{75-x}$ MEA system in which Wei et al. [25] reported that with increasing Co content, SFE is lowered, and the FCC phase stability is reduced. This destabilization of the FCC phase promotes the formation of the HCP phase during deformation. Particularly, the $Co_{45}Cr_{25}(FeNi)_{30}$ MEA contains a single metastable FCC solid solution phase, which undergoes TRIP upon deformation, resulting in the formation of a much harder HCP phase. This composition was specifically chosen because it sits on the border between a fully metastable FCC phase and a dual-phase FCC + HCP microstructure; any further increase in Co content beyond this point would result in the stabilization of the HCP phase, which would be detrimental to both processing and deformation behavior. The objective of this study is to understand how the microstructure and phase constitution of the as-printed $Co_{45}Cr_{25}(FeNi)_{30}$ MEA produced by PBF-LB, would influence the mechanical properties, with the expected TRIP behavior. We specifically investigated the impact of the nano-scaled HCP phase, present in the as-printed state (not present in the as-cast state). Using in-situ high-energy synchrotron X-ray diffraction (HEXRD) and extensive microstructural characterizations by electron backscatter diffraction (EBSD), we also explored the load partitioning that accompanied the phase transformation process which occurred upon deformation.

## 2. Materials and methods

### 2.1. Materials and fabrication

This study utilized pre-alloyed, gas-atomized spherical powder of the non-equiatomic $Co_{45}Cr_{25}Fe_{15}Ni_{15}$ medium entropy alloy (MEA), supplied by Höganäs AB. The powder had an average particle size (D50) of 32 μm and a D90 of 45 μm. The alloy was printed using EOS M100 PBF-LB machine equipped with 200W Yb-fiber laser. Extensive design of experiments (DOE) was performed to optimize the printing parameters for high density. The densities of the samples were measured on the optical micrographs of the polished samples, applying the contrast threshold technique using the ImageJ software [36]. Based on the DOE results, the samples used in this study were produced with 90W of laser power, 1010 mm/s of scan speed, 0.07 mm of hatch distance, 20 μm of layer thickness, with a stripe scan strategy and a stripe width of 5 mm with 67° scan rotation between subsequent layers.

X-ray computed tomography (XCT) on in-situ tensile samples was performed to evaluate the density of material at a v|tome|x L 300 CT scanner from General Electric. A tube voltage of 180 keV and a current of 45 μA were used, and the acquisition time for each projection was 2 s and the voxel size was 4 $\mu m^3$.

Fig. 1a shows the schematic of nomenclature of the samples used with respect to the building direction. The final density of the as-printed samples using the optimized parameters was > 99.9 %, confirmed by both optical microscopy and X-ray computed tomography (XCT, see Fig. 1b).

### 2.2. Characterization

#### 2.2.1. Microscopy and mechanical testing

The as-printed samples were metallographically prepared for microstructural characterizations by first grinding the samples using SiC emery sheets from 500 grit to 4000 grit. The ground samples were then electrochemically polished using the Struers A2 electrolyte to achieve a mirror-like finish. The preparation of TEM samples involved a two-step process. Initially, samples of approximately 1 mm thick were extracted along both vertical and horizontal cross sections from the as-printed bulk material. These extracted samples were then thinned down to a thickness of approximately 120 μm and punched into discs of 3 mm diameter. The final stage of the preparation involved twin-jet electrochemical polishing of the discs using Struers A2 electrolyte performed at −2 °C and 30 V until the hole is formed at the center of the sample.

The microstructural characterization of the samples was performed using multiple techniques. Back scattered electron (BSE) imaging, electron back scattered diffraction (EBSD) and transmission Kikuchi diffraction (TKD) of the samples were performed using Zeiss Gemini 450 scanning electron microscope (SEM) equipped with an EBSD detector (Symmetry, Oxford Instruments). The electron channeling contrast imaging (ECCI) was performed using acceleration voltage of 30 keV using a probe current of 10 nA and at working distance of approximately 6 mm. EBSD was performed at an acceleration voltage of 20 keV using a probe current 12 nA and at a step size of 0.15 μm. TKD was performed at an acceleration voltage of 30 keV using a probe current of 15 nA and at a step size of 18 nm.

In-situ EBSD combined with tensile testing was performed in GEMINI 1550 SEM equipped with the velocity detector. The in-situ EBSD and tensile tests were performed using a Kammrath & Weiss tensile stage mounted inside the SEM and at a strain rate of $\sim 2.5 \times 10^{-4}\ s^{-1}$. The EBSD acquisition was performed using an acceleration voltage of 20 keV and at a step size of 0.15 μm. Firstly, a carefully polished tensile sample was mounted onto the tensile stage inside the SEM and the EBSD data from the as-printed state was obtained at zero load. During the tensile testing, the loading was stopped at nominal strains of 15 %, 25 %, and 40 % to acquire EBSD data. Analysis of the all EBSD and TKD data presented in this study was performed using an open-source MATLAB toolbox, MTEX [11]. Ex-situ tensile testing was performed on the Kammrath & Weiss tensile stage to obtain mechanical properties of the alloy in the as-printed state, using the displacement control mode equivalent to a strain rate of $2.5 \times 10^{-4}\ s^{-1}$. Tensile samples of 4 mm in gauge length, 1.2 mm in thickness, and 2 mm in width were extracted from the as-printed samples, using electrical discharge machining

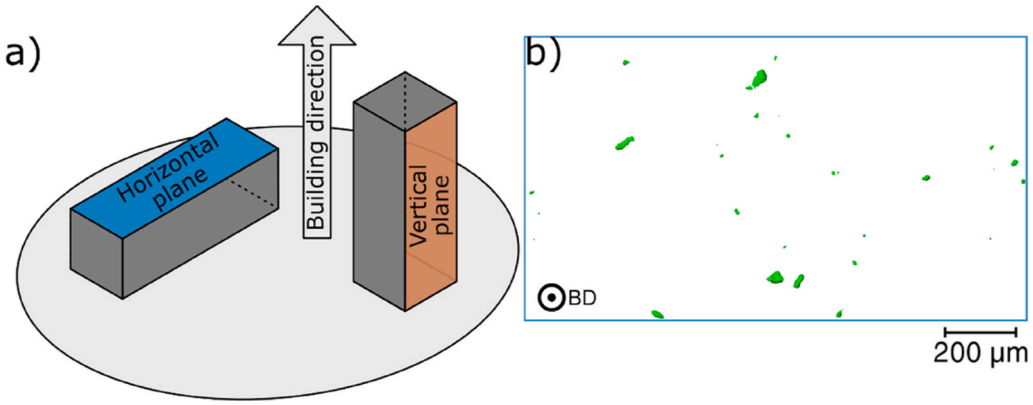


**Fig. 1.** a) schematic of the nomenclature of the samples used in this study with respect to the building direction and b) 3D rendering of porosity (in green) obtained by XCT, projected along the building direction.

(EDM). For each building direction, three samples were tested to ensure reproducibility, and the reported mechanical properties represent the averaged values.

### 2.2.2. *In-situ synchrotron X-ray diffraction studies*

Miniature dogbone shaped tensile samples were extracted from the as-printed samples, with a gauge length of 7 mm and thickness of 1.2 mm, using EDM. The extracted samples were then carefully mechanically ground and polished, finishing with colloidal suspension of 50 nm sized silica solution (OPS, Struers) to ensure that there was no deformed layer induced by grinding. The in-situ tensile tests were performed at a strain rate of $2.5 \times 10^{-4}$ $s^{-1}$ to a maximum nominal strain of 40 %. During the in-situ testing, images of samples were acquired at a time resolution of 1 s using a high-resolution camera. The strain was calculated using the digital image correlation technique (Vic-2D, Correlations Solutions). The HEXRD measurements (see Fig. 2) were carried out at the Swedish Materials Science beamline P21.2 at the Synchrotron Radiation Source at DESY: PETRA III, Hamburg, Germany [37]. The in-situ diffraction experiments were performed in transmission mode at 91 keV, with a spot size of 150 µm × 150 µm. The diffraction measurements were obtained continuously with a time resolution of 1 s. The acquisition of the 2D diffraction patterns was done using a Varex 4343CT flat panel detector. The calibration of the diffraction setup was performed using $CeO_2$ powder (NIST SRM 674b) [38]. The 2D diffraction images were integrated around the loading direction (LD) and transverse direction (TD) over the azimuthal angle in ranges of ±10° around each direction, to acquire the 1D diffraction patterns using the PyFAI module [39]. The single peak fitting of the integrated 1D patterns was performed using the in-house developed Python-based code. Firstly, centers of the peaks in the one 1D pattern were identified and the peak fitting was performed iteratively on all identified peaks using the pseudo-Voigt function. This process was repeated over all integrated 1D patterns in LD, and the peak fitting parameters: peak centers, intensities, and full width at half maximum (FWHM) were extracted. The d-spacing for all fitted peaks was calculated based on equation (1) [40]:

$$d_{(hkl)} = \frac{2^*\pi}{q} \tag{1}$$

Where $d_{(hkl)}$ is the lattice spacing for the hkl reflections and $q$ is the scattering vector modulus. The lattice strains for each reflection were measured using equation (2) [40]:

$$strain = \frac{d - d_0}{d_0} \tag{2}$$

where $d_0$ is the $d$-spacing for the reflections in the initial state, assumed to be the strain-free state neglecting any residual stress present in the material, and $d$ is the $d$-spacing obtained from Equation (1), measured every second.

Rietveld refinement was performed on the extracted 1D profiles using the GSAS II software [41]. A Chebyshev-I polynomial with an order of 3 was used to refine the background of the profile. The initial refinement was performed on the lattice parameters of the final profile,

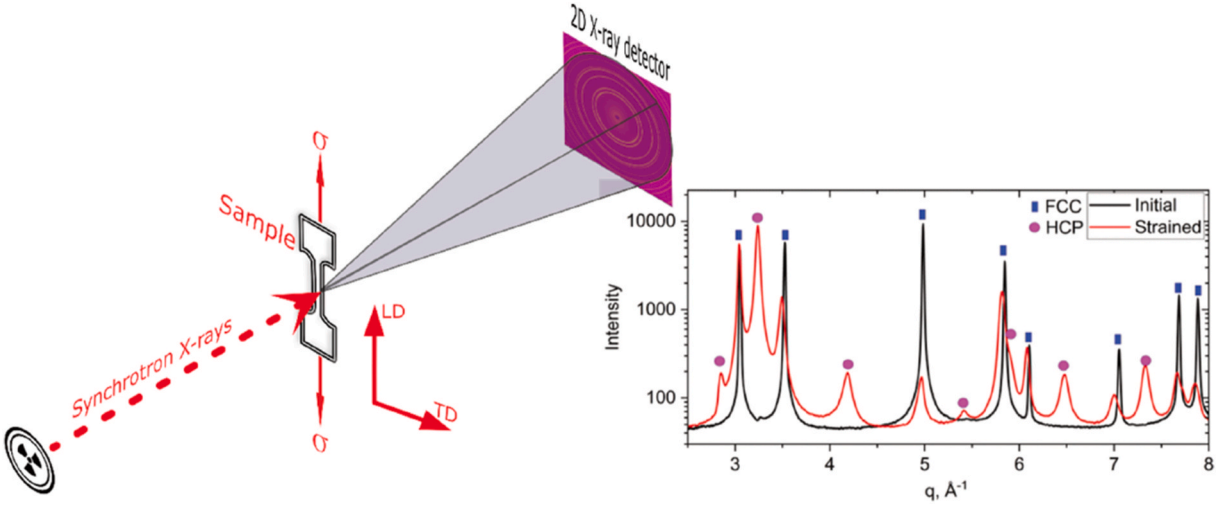


**Fig. 2.** Schematic of the experimental setup for the in-situ tensile tests performed using synchrotron X-Ray radiation.

considering both HCP and FCC phases. Subsequently, a cylindrical texture model was applied with a harmonic order of 12 for the FCC phase and 10 for the HCP phase. Initial estimates for the phase fractions were obtained from the EBSD results acquired from the fractured tensile sample. The isotropic macrostrain model was used to fit the peak broadening. Once the selected 1D profile was refined, sequential refinements were performed on all test profiles, starting from the final 1D profile (i.e., at 40 % normal strain), and the refinement results were exported to the next integrated profile. During the sequential refinement, the phase fractions, micro strains, hydrostatic and elastic strains, and texture parameters were refined with the above specified harmonic order.

## 3. Results

### 3.1. Microstructural characterization and ex-situ tensile tests

BSE-SEM images of the as-printed sample show a combination of typical PBF-LB epitaxial growth of coarse columnar grains along with small grains distributed across the microstructure (see Fig. 3a). Apart from the grain orientation contrast, a high density of band-like features were also observed in nearly every grain across the microstructure. The ECCI technique revealed that these band-like features were accompanied with significantly high density of defect substructures as shown in Fig. 3b.

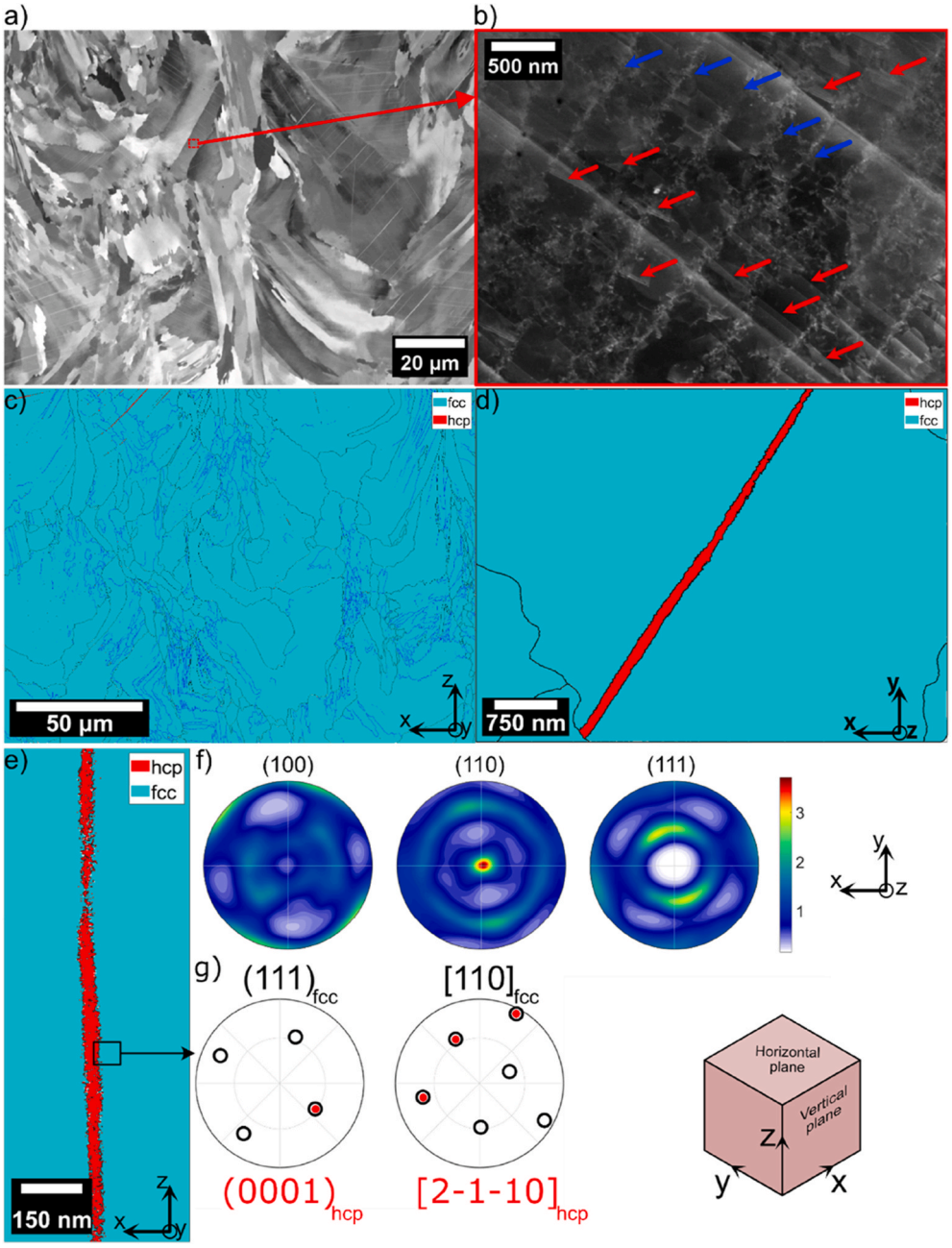


**Fig. 3.** a) BSE image of the as-printed sample parallel to the vertical plane and b) high magnification ECCI image showing a high density of dislocation substructures where red and blue arrows point to stacking faults and dislocation cells, respectively, c) low magnification EBSD phase map parallel to the building direction with black lines indicating the high angle grain boundaries (misorientation >10°) and blue lines indicating the low angle grain boundaries (misorientation angles between 2° and 10°). TKD phase map of the as-printed sample obtained from d) horizontal plane and e) vertical plane showing the presence nano-scaled HCP phase along with the FCC phase, f) pole figures for the FCC phase of the as-printed samples showing (110) texture parallel to the building direction and g) pole figures of the FCC and HCP phases (of the phases observed in Fig. 3e) showing the S-N orientation relationship, i.e., $(111)_{fcc}//(0001)_{hcp}$ and $[110]_{fcc}//[2\text{-}1\text{-}10]_{hcp}$ [45].

Fig. 3c–d shows the EBSD and TKD phase maps of the alloy in the as-printed state performed at low and high magnifications respectively. EBSD at low magnification shows that the entire microstructure was mostly the FCC phase with slight traces of the HCP phase. The poor indexing of the nano-scaled HCP in the EBSD was due to the limitation for the step size in EBSD. TKD was performed on the TEM samples at high magnifications to overcome the limitation of step size and it indexed the band-like features as the HCP phase. These features were observed in both the horizontal and vertical cross sections of the alloy as shown in Fig. 3d and e. A large area EBSD map of 3 mm by 3 mm was acquired parallel to the building direction to obtain representative statistics for the texture of the alloy. Pole figures of the FCC phase from that EBSD data are shown in Fig. 3f. The sample exhibits anisotropic texture with clear preferred orientations which is typical characteristic of the materials produced by PBF-LB due to the high thermal gradients and solidification velocities during the rapid melting and solidification process [42–44]. A strong clustering of orientations is observed in the (110) pole figure which indicates that the alloy exhibited strong (110) texture with a texture index of ~3.5 parallel to the building direction (here the building direction is into the plane of the pole figure) as shown in Fig. 3f.

The orientation relationship between the FCC and HCP phases was determined by analyzing the Euler angles of the HCP phase and its neighboring FCC phase obtained from TKD data. Based on these Euler angles, pole figures were calculated, which are shown in Fig. 3g. The pole figures in Fig. 3g correspond to the orientations of the FCC and HCP grains observed in Fig. 3e and they reveal that the HCP phase observed in the as-printed sample followed the $(111)_{fcc}//(0001)_{hcp}$ and $[110]_{fcc}//[2\text{-}1\text{-}10]_{hcp}$ orientation relationship to the FCC phase, which is the Shoji-Nishiyama (S-N) orientation relationship [45], as indicated by the coincidence of the FCC and HCP orientations.

Fig. 4a shows the true stress-true strain curve for the alloy in the as-printed state for the sample extracted from both horizontal and vertical directions. The summary of the tensile properties obtained from the *engineering* stress-strain data is shown in Table 1. The horizontal sample showed higher yield strength and ultimate tensile strength and slightly lower elongation to fracture as compared to the vertical sample. This is commonly observed in samples manufactured by PBF-LB due to the difference in the texture with respect to the building direction [46]. Fig. 4b shows the EBSD phase map of the fractured horizontal sample. The measured phase fractions were nearly 50 % for both the HCP and FCC phases. Fig. 4c shows the grains of FCC and HCP phases and their corresponding pole figures. The orientation relationship was determined from the pole figures for the FCC and HCP phases as shown in Fig. 4c. The overlapping of FCC and HCP orientations confirms that the deformation-induced HCP phase followed the S-N orientation relationship to the FCC phase, similar to the HCP phase observed in the as-printed state (see Fig. 3g).

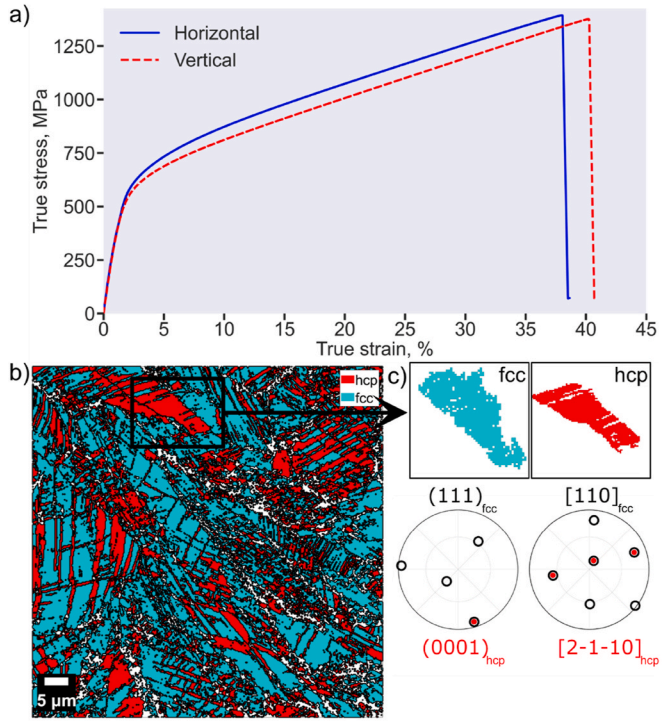


**Fig. 4.** a) True stress-strain plots of the as-printed samples extracted from vertical and horizontal planes; b) EBSD phase map of the horizontal sample after fracture, showing both the FCC and HCP phases, and c) grains of FCC phase and its neighboring HCP phase and their corresponding pole figures showing the S-N orientation relationship [45].

### 3.2. *In-situ HEXRD studies of tensile tests*

Fig. 5a shows the true stress-strain curve tested in both vertical and horizontal directions from the in-situ HEXRD experiments. Similar to the result from ex-situ tensile tests (Fig. 4a), compared to the vertical sample, the horizontal sample showed higher ultimate tensile strength, slightly higher yield stress and smaller elongation to failure. In fact, the horizontal sample fractured before reaching the set maximum nominal strain (40 %), while the vertical sample did not break until the end of the test.

Rietveld refinement of 1D profiles acquired from horizontal samples along the loading direction at the beginning of the tensile test (prior to straining, i.e., the as-printed state), and at the end of the tensile test, are shown in Fig. 5c–d. Fig. 5b shows the evolution of the HCP phase fraction measured from the sequential refinement as a function of true stress for the horizontal and vertical samples. The HCP phase fraction for the horizontal sample started to rise promptly upon straining, starting with 0.8 % in the as-printed state and reaching ~42 % at fracture. In the case of the vertical sample, the HCP fraction was observed to increase from the initial 1.5 % in the as-printed state, to nearly 60 % at the end of the test. Initially, the increase in the HCP volume fraction was observed to be faster in the horizontal sample. The evolution of the HCP fraction exhibited a steady increase up to the yield point for both horizontal and vertical samples. The vertical sample already exhibited a pronounced increase in HCP fraction below the yield point, whereas for the horizontal sample, the increase was delayed until after the yield point. The increase in the HCP phase fraction beyond the macroscopic yield was observed to be much faster for the vertical sample as compared to the horizontal sample. Two conclusions could be drawn from Fig. 5b. First, the HCP phase already existed in the as-printed state, confirming the martensite as seen from TKD in Fig. 3d–e. Second, the onset of TRIP was well below the yield point due to the increase in the phase fraction below the macroscopic yield. It seems that the volume fraction of the martensite in the as-printed state was slightly higher in the vertical sample, while it was much higher at fracture, compared to the horizontal sample. It should also be noted that, while the horizontal sample fractured well below the 40 % nominal strain during the in-situ test, the vertical sample did not undergo fracture resulting in a significantly higher fraction of the HCP phase.

Fig. 6 shows the lattice strain evolution as a function of true stress for selected HCP and FCC reflections obtained based on the peak fitting of

**Table 1**
Summary of tensile properties of the as-printed sample in both horizontal and vertical orientations for the $Co_{45}Cr_{25}(FeNi)_{30}$ MEA.

| Building direction | Yield strength (MPa) | Ultimate tensile strength (MPa) | Elongation to fracture (%) |
|---|---|---|---|
| Horizontal | 543 | 954 | 47 |
| Vertical | 514 | 921 | 49 |

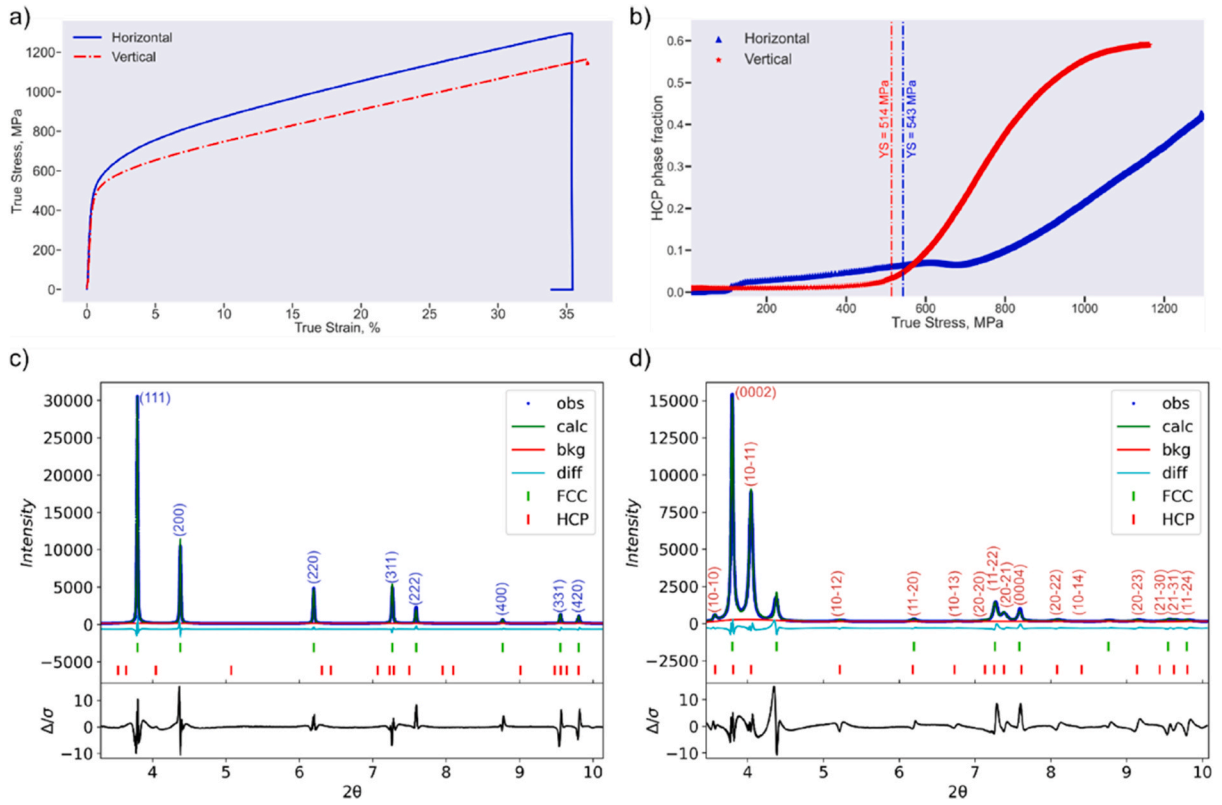


**Fig. 5.** a) True stress vs true strain curve obtained during the in-situ HEXRD experiment; b) the HCP phase fraction as a function of true stress obtained from the sequential Rietveld refinement of all 1D profiles, for the horizontal and vertical samples along the loading direction; Rietveld refinement on the 1D profiles for the horizontal samples along the loading direction from c) the as-printed state and d) the fractured sample.

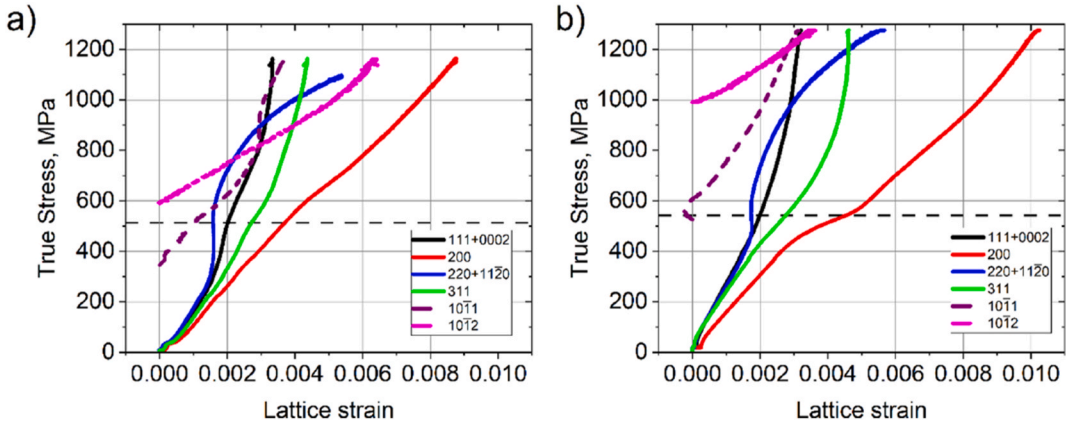


**Fig. 6.** Lattice strain evolution with applied true stress along LD for a) vertical sample and for b) horizontal sample. The black dashed line represents the yield strengths for horizontal and vertical samples, obtained from the ex-situ tensile tests (Table 1).

1D diffraction profiles from the in-situ HEXRD experiments, for both vertical and horizontal samples, along the loading direction. The dotted line shows the macroscopic yield stress of the material (from Table 1). Though the HCP phase was observed in the as-printed state, the volume fraction of it was too low for reliable fitting. Some of the HCP and FCC reflections overlapped, which made it difficult to distinguish between them reliably. This was particularly the case once a greater volume fraction of HCP was formed at high strain, whereby the behavior of the single peak fitting was increasingly dominated by the HCP phase (e.g., FCC (220) and HCP (11–20) reflections in Fig. 5c–d).

During the initial stage of loading, all FCC peaks were observed to sustain the strain elastically as evidenced by the linear correlation between stress and lattice strain in both vertical and horizontal orientations. The FCC (220), (111) and (311) peaks started to deviate from the elastic behavior and the correlation between stress and lattice strain became nonlinear as soon as the HCP phase started to form. Noticeably, this occurrence of nonlinearity happened well below the yield stress. On the other hand, the FCC (200) peak continued to exhibit a linear correlation between stress and lattice strain until a much later stage (i.e., larger strain), and the deviation from elastic behavior occurred just below the yield stress in the horizontal sample, while it was observed to be just above the yield stress for the vertical sample. This particular behavior of the FCC (200) peak is similar to what was previously seen during similar diffraction studies and was hypothesized to be a result of the textural evolution in the FCC phase during the dislocation slip [47–49].

The deviation from linear response for FCC peaks indicates the load partitioning during the tensile deformation, i.e., the load bore by FCC (220), (111) and (311) planes started to be shared with the HCP phase, as soon as the HCP (10–11) peak was observed, much before reaching the macroscopic yield stress. Beyond the macroscopic yield stress, the HCP (10–12) reflection was observed to form around 600 MPa and 1000 MPa in vertical and horizontal samples, respectively, indicating the progression of the FCC to HCP phase transformation during the tensile loading. The observed noticeable difference in the stress where the HCP (10–12) reflection was observed in vertical and horizontal samples could be attributed to variations in crystallographic orientation and texture within the material, and the different amount of HCP phase existing in the as-printed state. Further loading in samples from both printing directions resulted in the sharp increase of the lattice strain for the HCP (10–12) plane, along with the unloading for the HCP (10–11) plane particularly in the vertical sample. This indicates the load partitioning among the HCP planes. As previously mentioned, FCC (220) and HCP (11–20) peak positions overlapped significantly. Once the FCC (220) peak started to deviate from the linear response, the load sharing from FCC (200) to HCP (11–20) planes occurred. Initially, the FCC (220) reflection showed similar behavior to the rest of the FCC reflections, but once the HCP (11–20) peak was formed, it deviated and was dominated by the loading behavior of the HCP (11–20) peak, accompanying a sharp increase of lattice strain due to the phase transformation.

Fig. 7 shows the normalized intensity vs. true strain and full width at half maximum (FWHM) vs. true stress of selected HCP and FCC reflections. The continuous decrease of intensity of FCC peaks corresponded to the phase transformation starting from the very beginning of the test. However, the FCC (111) peak intensity first decreased and then increased, which suggests that the HCP (0002) peak dominated at high strain (overlapping peaks). The HCP (10–12) peak intensity increased to a maximum around 14 % true strain, then decreased at higher true strain. The initial intensity increase in the HCP (10–12) peak was associated with the increase in the HCP phase fraction, while the decrease of the intensity was possibly due to the reorientation resulting in the 86.6° rotation of the planes due to the extension twinning in the HCP phase [49]. The intensity of the HCP (10–11) peak increased throughout the test. FWHM provides useful information about the strain accumulation inside the material. From Fig. 7b, there was a slight increase of FWHM for the FCC phase, well before reaching the macroscopic yield point, indicating the start of earlier slip in the FCC phase. After the yield point, FWHM increased rapidly, which is an indication of increasing stacking faults and dislocation densities.

### 3.3. In-situ EBSD studies of tensile tests

Fig. 8 shows the EBSD phase maps for the vertical sample that was subjected to in-situ tensile tests, at 0 %, 15 %, 25 % and 40 % nominal strain, respectively. In the as-printed state, as previously discussed in section 3.1, the size of the HCP phase was observed to be nano-scaled. The step size used for EBSD acquisition was too high to distinguish and confidently index the nano-scaled HCP phase, and hence almost no HCP phase was observed in the as-printed sample. With an increase in the strain to 15 %, the phase transformation increased the HCP phase fraction to 4 %. At 25 % of nominal strain, the HCP phase fraction increased significantly to nearly 33 %, and finally at 40 % nominal strain the measured HCP phase fraction was nearly 50 %. This change in the HCP phase fraction corresponded well with the postmortem phase fraction as shown in Fig. 4b.

The evolution of phase fractions from the in-situ EBSD studies and in-situ HEXRD experiments shows notable differences at certain strain levels, as seen in Figs. 5b and 8. These variations arise due to the inherent differences in how the two techniques probe the material: EBSD is a surface-sensitive technique with a localized sampling region, while HEXRD provides bulk phase fraction measurements by integrating diffraction signals from a much larger volume across the gauge section.

For example, at low strains, HEXRD detects a significantly higher HCP phase fraction than EBSD, particularly at 15 % strain (HEXRD ~35 % vs. EBSD ~4 %). This discrepancy arises because the early-stage HCP phase is nano-scaled and difficult to resolve with EBSD due to step size limitations and overlapping diffraction patterns. As deformation progresses, the HCP phase coarsens, improving detectability in EBSD. At high strains, in addition to differences in sampling volume, EBSD indexing quality is further affected by increasing lattice distortion. The high strain state leads to severe lattice misorientation and local deformation, reducing the ability of EBSD to accurately index the HCP phase, as evident from Fig. 8. This effect contributes to the differences observed between HEXRD and EBSD at later deformation stages.

Despite these differences, EBSD provides better visualization of the progression of martensitic transformation throughout the deformation process. Additionally, the phase fractions measured from EBSD serve as a good starting estimate for Rietveld refinement in HEXRD analysis, helping to improve the accuracy of phase quantification.

## 4. Discussion

### 4.1. Influence of the PBF-LB process conditions on the phase transformation

When a low SFE alloy with the ability to undergo TRIP is deformed, the FCC to HCP phase transformation is typically linked to the formation of shear bands during the plastic deformation [50,51]. Shear bands are often known to form in the regions where the deformation is highly localized and intense, typically within the FCC phase. This localized shear deformation in the FCC phase leads to the generation of substantial number of dislocations and stacking faults, particularly concentrated

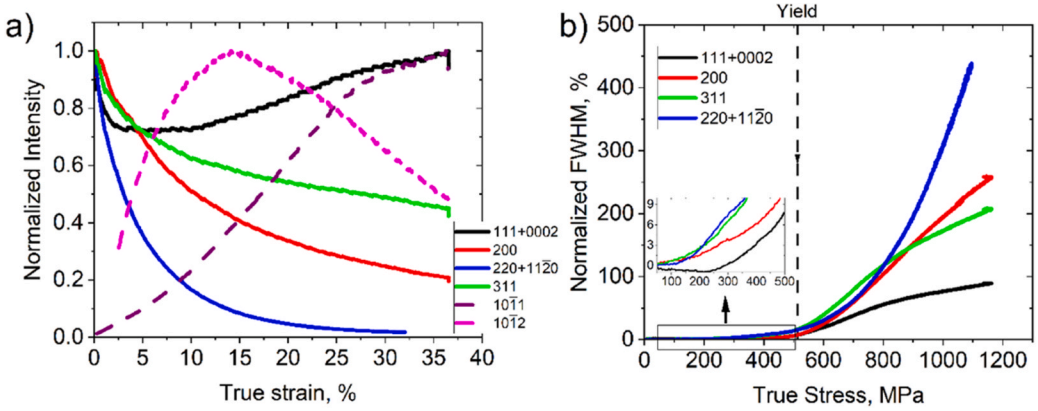


**Fig. 7.** a) Normalized intensity as a function of true strain and b) normalized FWHM as a function of true stress for the vertical sample along LD.

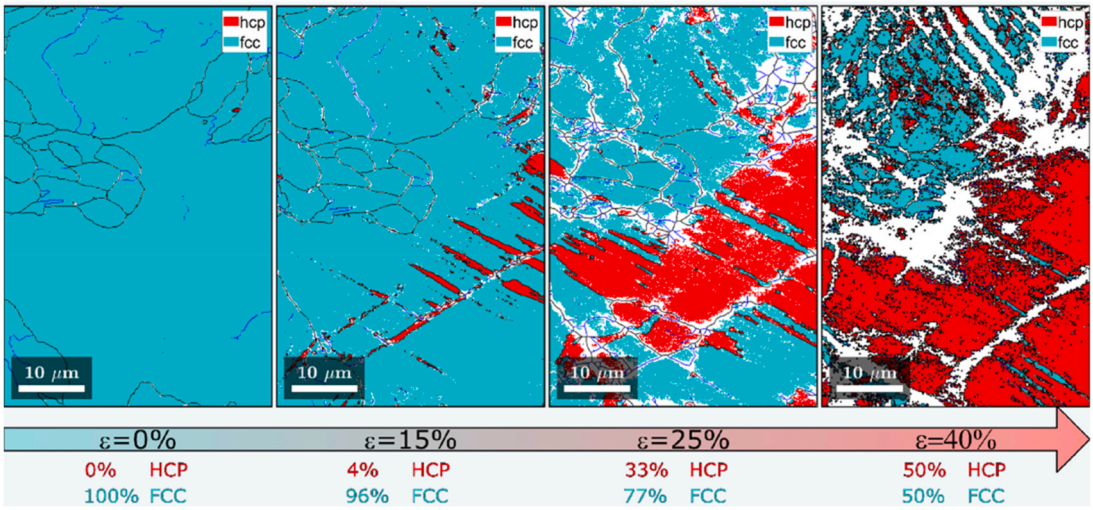


**Fig. 8.** EBSD phase maps from the in-situ tensile tests showing the evolution of FCC and HCP phase fractions with increasing normal strain.

at the shear bands [19,31]. These stacking faults and shear bands can serve as nucleation sites for the formation of HCP nuclei which grow upon further deformation [21,23,52–55]. As deformation proceeds, more HCP phase forms leading to significant strain hardening of the alloy. Hence, the starting microstructure and dislocation densities play a crucial role in the TRIP behavior and determine the extent of phase transformation of these alloys [56].

The alloys manufactured by PBF-LB typically consist of significantly higher dislocation density (in the form of dislocation cells) as compared to the traditional wrought alloys, due to subsequent thermal cycling inherent to the layer-by-layer manufacturing [33–35]. In the case of the present alloy in the as-printed state (see Fig. 3a–b) along with the characteristic dislocation cells, a high density of dislocation substructures was also observed. The presence of this high density of dislocation substructures in the as-printed state would be beneficial for the martensite formation upon deformation. Along with the high dislocation densities, the nano-scaled HCP phase was observed in the FCC phase in the as-printed state. The presence of this initial HCP phase could act as nucleating points for the deformation induced HCP, thereby enhancing the strain hardening behavior by providing an alternative pathway for the growth of the HCP phase during deformation. This suggests that the formation of deformation induced martensite (HCP) could occur well below the macroscopic yield point, resulting in the stress-induced transformation [21].

Though there was a difference in the mechanical properties with respect to the different building directions, the amount of such difference was significantly lower than that usually reported in literature [42,46]. This could be due to the alloy's inherently low SFE resulting in the material undergoing strain hardening along with the presence of the ε-martensite in the as-printed state. Another interesting observation from the tensile tests was that all tested samples fractured at UTS, and no post-necking elongation was observed. This behaviour is also very typical to the alloys that undergo TRIP, thereby resulting in the formation of brittle martensitic phase [28,31,49].

### 4.2. Load partitioning behavior during tensile testing

In general, along the loading direction, FCC reflections exhibit linear stress-strain response with the general trend of elastic anisotropy exhibited by polycrystalline FCC materials, whereby (200) planes are the softest planes [47–49,57] while (111) are the stiffest. However, here all FCC reflections except for FCC (200) showed a deviation from linearity well below the macroscopic yield point (Fig. 6a–b). The degree of non-linearity as described in section 3.2, increased in the order from FCC (200), (311), (111) to (220), and this was often seen as plastic anisotropy in single-phase FCC materials [47,48,58]. Therefore, this observation suggests that some degree of plastic deformation already occurred for the FCC phase significantly below the macroscopic yield stress. The origin of the early yielding in the FCC phase may be attributed to the presence of microscopic residual strains between different grain families, as reported by Wang et al. [59] in PBF-LB 316L. For the vertical sample this nonlinearity occurred at stresses where the HCP (10–11) reflection could be reliably fitted (Fig. 6a). The lattice strain of the HCP (10–11) increased linearly to the macroscopic yield point, where FCC peaks continued to sustain lattice strain with increasing load. Therefore, there may be some contribution of the interphase stresses between the FCC and the HCP phases to the early yielding [60]. For the horizontal sample, this nonlinearity occurred at similar stress, however, the HCP phase was initially not reliability fitted and thereafter did not appear to sustain load until the macroscopic yield point was almost reached (Fig. 6b). Also, the HCP (10–12) reflection appeared as the applied stress increased, due to extensive phase transformation. Its lattice strain rapidly increased while most of the FCC planes started unloading. Apart from the difference in texture, originated from the different orientations of the main sample axis to the building direction, the general trend of the microscopic strain behavior was similar for horizontal and vertical samples.

The nano-scaled HCP observed in the as-printed samples was expected to accelerate the TRIP kinetics during the deformation. The in-situ synchrotron tensile tests validated the hypothesis of the stress induced transformation, where the FCC phase exhibited nonlinear stress-strain response far below the macroscopic yield stress. This nonlinearity was considered as a mixture of plastic anisotropy of the FCC phase occurring early before yielding, due to the presence of both intergranular and interphase residual strains, and the load partitioning to the HCP phase, particularly to the HCP (10–11) planes, which was observed to form well below the macroscopic yield point.

## 5. Conclusions

Our study revealed the formation of characteristic dislocation cells and a high density of defect substructures in a $Co_{45}Cr_{25}(FeNi)_{30}$ MEA manufactured using PBF-LB. The high cooling rate inherent to PBF-LB led to the formation of nano-scaled martensite alongside the FCC phase. The FCC phase exhibited a strong (110) texture along the building direction. Ex-situ tensile testing demonstrated yield strengths of 547 MPa in the horizontal direction and 512 MPa in the vertical direction, with significantly reduced anisotropy compared to other PBF-LB

alloys due to the inherent strain hardening ability of the alloy.

In-situ HEXRD and EBSD tensile testing revealed that the high dislocation density and nano-scaled HCP phase in the as-printed state were responsible for the stress-induced martensitic transformation. Our findings indicated that the onset of the martensitic transformation occurred below the macroscopic yield points in both vertical and horizontal samples, as evidenced by the appearance of the (10–11) reflection for the HCP phase. It is noted that, while the most prominent increase in the HCP (10–11) reflection's lattice strain in the horizontal sample is observed closer to the yield point, early signs of the transformation, such as the deviation from linearity of FCC reflections and the increase in martensitic phase fraction (Fig. 5b), are evident at lower stress levels. The observed deviation from the linear response between stress and strain for FCC reflections in both vertical and horizontal samples was attributed to a combination of plastic anisotropy of the FCC phase and the load transfer to the HCP phase, with the latter playing a more dominant role.

The presence of nano-scaled HCP phase in the as-printed state was also seen as a possible source for the early onset of the non-linear lattice strain behavior as a function of the applied stress. The non-linear lattice strain behavior is thought to correlate with the strain hardening of the alloy, which is stronger in the vertical sample which tends to be softer than the horizontal sample. The high cooling rate offered by PBF-LB therefore provides a potential route to contribute to reducing plastic anisotropy inherent to additive manufactured materials caused by texture, in metastable materials where TRIP is known to occur.

## CRediT authorship contribution statement

**Sri Bala Aditya Malladi:** Writing – review & editing, Writing – original draft, Visualization, Validation, Software, Methodology, Investigation, Formal analysis, Data curation, Conceptualization. **Tatiana Mishurova:** Writing – review & editing, Writing – original draft, Visualization, Investigation, Formal analysis, Data curation. **Vishnu Anilkumar:** Writing – review & editing, Visualization, Investigation, Data curation. **Bharat Mehta:** Writing – review & editing, Methodology, Investigation. **Alexander Evans:** Writing – review & editing, Writing – original draft, Visualization, Validation, Supervision, Investigation, Formal analysis, Conceptualization. **Kumar Babu Surreddi:** Writing – review & editing, Methodology, Investigation. **Malte Blankenburg:** Methodology, Investigation. **Ulrich Lienert:** Methodology, Investigation. **Giovanni Bruno:** Writing – review & editing. **Sheng Guo:** Writing – review & editing, Writing – original draft, Supervision, Formal analysis, Conceptualization. **Lars Nyborg:** Writing – review & editing, Supervision, Funding acquisition.

## Declaration of competing interest

The authors declare that they have no known competing financial interests or personal relationships that could have appeared to influence the work reported in this paper.

## Acknowledgements

This study was performed as part of the strategic innovation program, Competence Centre for Additive Manufacture – Metal (CAM [2]) (Grant number: 2022-03076) with the support from Vinnova and from Swedish Research Council (Grant number: 2020-0619). The industrial partner Höganäs AB is greatly acknowledged for their support. We acknowledge DESY (Hamburg, Germany), a member of the Helmholtz Association HGF, for the provision of experimental facilities and allocation of the beamtime for proposal I-20220972. The authors would like to thank Andrea Fantin (BAM) for a fruitful discussion.

## Data availability

Data will be made available on request.

## References

[1] M.H. Tsai, J.W. Yeh, High-entropy alloys: a critical review, Mater Res Lett 2 (2014) 107–123.
[2] S. Guo, Q. Hu, C. Ng, C.T. Liu, More than entropy in high-entropy alloys: forming solid solutions or amorphous phase, Intermetallics 41 (2013) 96–103.
[3] E.P. George, D. Raabe, R.O. Ritchie, High-entropy alloys, Nat. Rev. Mater. 4 (2019) 515–534, 2019 4:8.
[4] E.J. Pickering, N.G. Jones, High-entropy alloys: a critical assessment of their founding principles and future prospects, Int. Mater. Rev. 61 (2016) 183–202.
[5] S. Guo, Phase Selection Rules for Cast High Entropy Alloys: an Overview, vol. 31, 2015, pp. 1223–1230, https://doi.org/10.1179/1743284715Y.0000000018.
[6] A. Gali, E.P. George, Tensile properties of high- and medium-entropy alloys, Intermetallics 39 (2013) 74–78.
[7] B. Schuh, et al., Mechanical properties, microstructure and thermal stability of a nanocrystalline CoCrFeMnNi high-entropy alloy after severe plastic deformation, Acta Mater. 96 (2015) 258–268.
[8] A. Semenyuk, et al., Effect of nitrogen on microstructure and mechanical properties of the CoCrFeMnNi high-entropy alloy after cold rolling and subsequent annealing, J. Alloys Compd. 888 (2021) 161452.
[9] I. Moravcik, et al., Nitrogen interstitial alloying of CoCrFeMnNi high entropy alloy through reactive powder milling, Entropy 21 (2019) 1–7.
[10] J. Zhang, et al., Strengthening by customizing microstructural complexity in nitrogen interstitial CoCrFeMnNi high-entropy alloys, J. Alloys Compd. 901 (2022) 163483.
[11] D. Xu, M. Wang, T. Li, X. Wei, Y. Lu, A critical review of the mechanical properties of CoCrNi-based medium-entropy alloys, Microstructures 2 (2022) 2022001.
[12] H. Huang, et al., Strengthening CoCrNi medium-entropy alloy by tuning lattice defects, Scr. Mater. 188 (2020) 216–221.
[13] J.P. Liu, et al., Superior strength-ductility CoCrNi medium-entropy alloy wire, Scr. Mater. 181 (2020) 19–24.
[14] D.E. Jodi, N. Choi, J. Park, N. Park, Mechanical performance improvement by nitrogen addition in N-CoCrNi compositionally complex alloys, Metall. Mater. Trans. 51 (2020) 3228–3237, 2020 51:6.
[15] I. Moravcik, et al., Interstitial doping enhances the strength-ductility synergy in a CoCrNi medium entropy alloy, Mater. Sci. Eng., A 781 (2020) 139242.
[16] I. Moravcik, et al., Yield strength increase of a CoCrNi medium entropy alloy by interstitial nitrogen doping at maintained ductility, Scr. Mater. 178 (2020) 391–397.
[17] A.J. Zaddach, C. Niu, C.C. Koch, D.L. Irving, Mechanical properties and stacking fault energies of NiFeCrCoMn high-entropy alloy, JOM 65 (2013) 1780–1789.
[18] S. Huang, et al., Twinning in metastable high-entropy alloys, Nat. Commun. 9 (2018) 1–7, 2018 9:1.
[19] Z. Li, K.G. Pradeep, Y. Deng, D. Raabe, C.C. Tasan, Metastable high-entropy dual-phase alloys overcome the strength–ductility trade-off, Nature 534 (2016) 227–230, 2016 534:7606.
[20] J. Su, X. Wu, D. Raabe, Z. Li, Deformation-driven bidirectional transformation promotes bulk nanostructure formation in a metastable interstitial high entropy alloy, Acta Mater. 167 (2019) 23–39.
[21] D. Fahr, Stress- and strain-induced formation of martensite and its effects on strength and ductility of metastable austenitic stainless steels, Metall. Trans. A 2 (1971) 1883–1892.
[22] Olson, G. B. & Cohen, *M. A* General mechanism of martensitic nucleation= part I. General Concepts and the FCC HCP Transformation.
[23] G.B. Olson, M. Cohen, A general mechanism of martensitic nucleation: part III. Kinetics of martensitic nucleation, Metall. Trans. A 7 (1976) 1915–1923.
[24] S. Basu, Z. Li, K.G. Pradeep, D. Raabe, Strain rate sensitivity of a TRIP-Assisted dual-phase high-entropy alloy, Front Mater. 5 (2018) 379083.
[25] D. Wei, et al., Novel Co-rich High Entropy Alloys with Superior Tensile Properties, vol. 7, 2019, pp. 82–88.
[26] D. Raabe, Z. Li, D. Ponge, Metastability alloy design, MRS Bull. 44 (2019) 266–272.
[27] J. Su, D. Raabe, Z. Li, Hierarchical microstructure design to tune the mechanical behavior of an interstitial TRIP-TWIP high-entropy alloy, Acta Mater. 163 (2019) 40–54.
[28] Z. Wang, W. Lu, D. Raabe, Z. Li, On the mechanism of extraordinary strain hardening in an interstitial high-entropy alloy under cryogenic conditions, J. Alloys Compd. 781 (2019) 734–743.
[29] W. Lu, et al., Bidirectional transformation enables hierarchical nanolaminate dual-phase high-entropy alloys, Adv. Mater. 30 (2018) 1804727.
[30] G. Wu, et al., Crystal–glass high-entropy nanocomposites with near theoretical compressive strength and large deformability, Adv. Mater. 32 (2020) 2002619.
[31] P. Agrawal, et al., Metastable high entropy alloys: an excellent defect tolerant material for additive manufacturing, Mater. Sci. Eng., A 826 (2021) 142005.
[32] A. Basak, S. Das, Epitaxy and microstructure evolution in metal additive manufacturing, Annu. Rev. Mater. Res. 46 (2016) 125–149, https://doi.org/10.1146/annurev-matsci-070115-031728. Preprint at.
[33] Y. Liu, J. Zhang, Z. Pang, Numerical and experimental investigation into the subsequent thermal cycling during selective laser melting of multi-layer 316L stainless steel, Opt Laser. Technol. 98 (2018) 23–32.

[34] Y. Liu, Z. Pang, J. Zhang, Comparative study on the influence of subsequent thermal cycling on microstructure and mechanical properties of selective laser melted 316L stainless steel, Appl. Phys. Mater. Sci. Process 123 (2017) 1–10.
[35] Y. Wu, S. Zhang, X. Cheng, H. Wang, Investigation on solid-state phase transformation in a Ti-47Al-2Cr-2V alloy due to thermal cycling during laser additive manufacturing process, J. Alloys Compd. 799 (2019) 325–333.
[36] J. Schindelin, et al., Fiji: an open-source platform for biological-image analysis, Nat. Methods 9 (2012) 676–682, 2012 9:7.
[37] Z. Hegedüs, et al., Imaging modalities at the Swedish materials science beamline at PETRA III, IOP Conf. Ser. Mater. Sci. Eng. 580 (2019) 012032.
[38] Choquette, S. J. Certificate of Analysis Standard Reference Material 674b X-Ray Powder Diffraction Intensity Set (Quantitative Powder Diffraction Standard).
[39] C. Hanmandlu, et al., PyFAI, a versatile library for azimuthal regrouping, J. Phys. Conf. Ser. 425 (2013) 202012.
[40] J. Bolze, M. Gateshki, Highly versatile laboratory X-ray scattering instrument enabling (nano-)material structure analysis on multiple length scales by covering a scattering vector range of almost five decades, Rev. Sci. Instrum. 90 (2019) 123103.
[41] B.H. Toby, R.B. Von Dreele, GSAS-II: the Genesis of a Modern open-source all Purpose Crystallography Software Package, 2013, pp. 544–549, urn:issn:0021-8898 46.
[42] J. Schröder, et al., Understanding the impact of texture on the micromechanical anisotropy of laser powder bed fused inconel 718, J. Mater. Sci. 57 (2022) 15036–15058.
[43] J.J. Marattukalam, et al., The effect of laser scanning strategies on texture, mechanical properties, and site-specific grain orientation in selective laser melted 316L SS, Mater. Des. 193 (2020).
[44] M.-S. Pham, B. Dovgyy, P.A. Hooper, C.M. Gourlay, A. Piglione, The role of side-branching in microstructure development in laser powder-bed fusion, Nat. Commun. 11 (2020) 1–12, 2020 11:1.
[45] Crystallography of Martensite (General), Martensitic Transformation, 1978, pp. 14–134, https://doi.org/10.1016/B978-0-12-519850-9.50007-7.
[46] A. Charmi, et al., Mechanical anisotropy of additively manufactured stainless steel 316L: an experimental and numerical study, Mater. Sci. Eng., A 799 (2021) 140154.
[47] S.F. Liu, et al., Transformation-reinforced high-entropy alloys with superior mechanical properties via tailoring stacking fault energy, J. Alloys Compd. 792 (2019) 444–455.
[48] M. Naeem, et al., Cooperative deformation in high-entropy alloys at ultralow temperatures, Sci. Adv. 6 (2020) 4002–4029.
[49] E. Polatidis, et al., Unveiling the interplay of deformation mechanisms in a metastable high entropy alloy with tuned composition using synchrotron X-ray diffraction, Mater. Today Commun. 30 (2022) 103155.
[50] J. Talonen, H. Hänninen, Formation of shear bands and strain-induced martensite during plastic deformation of metastable austenitic stainless steels, Acta Mater. 55 (2007) 6108–6118.
[51] L.E. Murr, K.P. Staudhammer, S.S. Hecker, Effects of strain state and strain rate on deformation-induced transformation in 304 stainless steel: part II. Microstructural study, Metall. Trans. A 13 (1982) 627–635.
[52] Y.H. Jo, et al., FCC to BCC transformation-induced plasticity based on thermodynamic phase stability in novel V10Cr10Fe45CoxNi35−x medium-entropy alloys, Sci. Rep. 9 (2019) 1–14, 2019 9:1.
[53] H. Kashani, M.S. Laridjani, A. Amadeh, M. Khodagholi, S. Ahmadzadeh, The influence of volumetric dilution on the strain induced $\gamma \rightarrow \varepsilon$ martensitic transformation in GTAW processed co–cr–mo alloy, Mater. Sci. Eng., A 478 (2008) 38–42.
[54] A. Mani, H.F. Salinas-Rodriguez & Lopez, Deformation induced FCC to HCP transformation in a Co–27Cr–5Mo–0.05C alloy, Mater. Sci. Eng., A 528 (2011) 3037–3043.
[55] G.N. Haidemenopoulos, A.N. Vasilakos, Modelling of austenite stability in low-alloy triple-phase steels, Steel Res. 67 (1996) 513–519.
[56] A.D.J. Saldívar García, A. Maní Medrano, A. Salinas Rodríguez, Effect of solution treatments on the FCC/HCP isothermal martensitic transformation in Co-27Cr-5Mo-0.05C aged at 800°C, Scr. Mater. 40 (1999) 717–722.
[57] J.N. Wagner, M. Hofmann, R. Wimpory, C. Krempaszky, M. Stockinger, Microstructure and temperature dependence of intergranular strains on diffractometric macroscopic residual stress analysis, Mater. Sci. Eng., A 618 (2014) 271–279.
[58] X. Fang, et al., Superior strength-ductility synergy by hetero-structuring high manganese steel, Mater Res Lett 8 (2020) 417–423.
[59] Y.M. Wang, et al., Additively manufactured hierarchical stainless steels with high strength and ductility, Nat. Mater. 17 (2017) 63–71, 2017 17:1.
[60] I.V. Kireeva, Y.I. Chumlyakov, A.A. Saraeva, A.V. Vyrodova, Physical factors controlling large shape memory effect in FCC ↔ HCP martensitic transformation in CrMnFeCoNi high-entropy-alloy single crystals, Metals 13 (2023) 1755, 2023, Vol. 13, Page 1755.